Key Points:
- A comparison tool has been developed by mapping global GPS TEC and large coverage of scintillations together on MLAT/MLT coordinates
- σ_φ were larger than S_4 at the edges of the irregularities associated with bursty flows or flow reversals with large density gradients
- S_4 were much larger than σ_φ in the auroral oval, most likely caused by particle precipitations around the exiting polar cap patches

Correspondence to:
Q.-H. Zhang,
zhangqinghe@sdu.edu.cn

A comparison between large-scale irregularities and scintillations in the polar ionosphere

Y. Wang[1], Q.-H. Zhang[1], P. T. Jayachandran[2], M. Lockwood[3], S.-R. Zhang[4], J. Moen[5], Z.-Y. Xing[1], Y.-Z. Ma[1], and M. Lester[6]

[1]Shandong Provincial Key Laboratory of Optical Astronomy and Solar-Terrestrial Environment, Institute of Space Sciences, Shandong University, Weihai, China, [2]Physics Department, University of New Brunswick, Fredericton, New Brunswick, Canada, [3]Department of Meteorology, University of Reading, Reading, UK, [4]Haystack Observatory, Massachusetts Institute of Technology, Cambridge, Massachusetts, USA, [5]Department of Physics, University of Oslo, Oslo, Norway, [6]Department of Physics and Astronomy, University of Leicester, Leicester, UK

Abstract A comparison tool has been developed by mapping the global GPS total electron content (TEC) and large coverage of ionospheric scintillations together on the geomagnetic latitude/magnetic local time coordinates. Using this tool, a comparison between large-scale ionospheric irregularities and scintillations is pursued during a geomagnetic storm. Irregularities, such as storm enhanced density, middle-latitude trough, and polar cap patches, are clearly identified from the TEC maps. At the edges of these irregularities, clear scintillations appeared but their behaviors were different. Phase scintillations (σ_φ) were almost always larger than amplitude scintillations (S_4) at the edges of these irregularities, associated with bursty flows or flow reversals with large density gradients. An unexpected scintillation feature appeared inside the modeled auroral oval where S_4 were much larger than σ_φ, most likely caused by particle precipitations around the exiting polar cap patches.

1. Introduction

The fluctuations in the spatial propagating radio wave signals (like their amplitude and phase) are one of the first known effects of space weather, which is called scintillation [e.g., *Hey et al.*, 1946]. This is due to the radio signals be disturbed or interrupted when they are passing through the ionospheric irregularities, which are often associated with large density gradients resulting in clear scintillations to the satellite navigation, positioning, and communication [e.g., *Weber et al.*, 1986; *Mitchell et al.*, 2005; *Moen et al.*, 2013]. In the polar ionosphere, there are many large-scale irregularities, such as storm enhanced density (SED)/tongue of ionization (TOI) [*Foster et al.*, 2005, 2007], middle-latitude trough, and polar cap patches [e.g., *Zhang et al.*, 2011, 2013a, 2015]. The SED, as a plume of very high concentration plasma around the noon sector, drifts from the low-latitude sunlit region in the afternoon sector toward higher latitudes by the poleward directed subauroral polarization stream (SAPS) electric fields, entering the polar cap region and forming a TOI [*Foster*, 2008]. The SAPS is characterized by the bursty sunward return flow, which is produced by the modulation of night-side reconnection and overlaps with the middle-latitude trough [*Foster and Burke*, 2002]. *Zhang et al.* [2013a, 2015] found that these bursty sunward return flows or SAPS could carry low-density plasma (trough) toward the cusp region along the dawnside and/or duskside return convection cell, thereby injecting low-density plasma into the convection throat and cutting the SED plume into polar cap patches. We will refer to the interaction area between the bursty sunward return flows or SAPS and the SED as the "SED segmented area." The polar cap patches are islands of high number density *F* region ionospheric plasma, which are surrounded by plasma of half the concentration or less [e.g., *Crowley*, 1996; *Carlson*, 2012; *Zhang et al.*, 2011, 2013b]. After formation, the polar cap patches move along the flow streamlines of the Dungey convection cycle [*Dungey*, 1961; *Oksavik et al.*, 2010; *Hosokawa et al.*, 2009; *Zhang et al.*, 2013a, 2015] and transpolar evolution from the dayside to the nightside. They have been found exiting the polar cap and entering the nightside auroral oval, in a manner modulated by the nightside reconnection rate, and evolving to dayside in the sunward return flow region [*Zhang et al.*, 2013a, 2015].

At the edges of these large-scale irregularities, there are often very high density gradients with different small-scale size irregularities, generated by various instabilities, such as flow shear instability (or Kelvin-Helmholtz instability (KHI)) and/or gradient drift instability (GDI) [*Basu et al.*, 1990, 1994, 1998; *De Franceschi et al.*, 2008; *Moen et al.*, 2013]. Thus, clear scintillations often appear at the edges of the large-scale irregularities. The

scintillations are generally divided into amplitude and phase scintillations based on the behavior of the disturbance of the received signals. Previous studies suggested that amplitude scintillations, quantified by S_4 index, are mainly caused by tens of meters to hundreds of meters scale size irregularities, while phase scintillations, quantified by σ_φ index, are mainly caused by hundreds of meters to some kilometers scale size irregularities, which are above the Fresnel radius (a few hundred meters for Global Positioning System (GPS) signals) [e.g., *Kintner et al.*, 2007; *Alfonsi et al.*, 2011; *van der Meeren et al.*, 2014; *Oksavik et al.*, 2015]. Several publications have investigated the relationships between plasma irregularities and scintillations in the polar ionosphere, trying to understand the generation mechanisms of the ionospheric scintillations around the edges of different large-scale irregularities [*Prikryl et al.*, 2010; *Moen et al.*, 2013; *Oksavik et al.*, 2015]. *Mitchell et al.* [2005] reported that both amplitude and phase scintillations coexisted with the strong gradients in total electron content (TEC) at the edge of polar cap patches near the nightside auroral oval during the Halloween storm in October 2003. However, only phase scintillation was observed at the tip region of TOI [*van der Meeren et al.*, 2014]. *Oksavik et al.* [2015] reported severe phase scintillation and strong irregularities associated with bright poleward moving auroral forms around cusp region. *Jin et al.* [2015] is a statistical study of the cusp auroral and GPS scintillations and proposed that the phase scintillations are sensitive to a combination of both the auroral precipitation and the transported higher density plasma from sunlit part of the ionosphere. Some previous studies also suggested that the amplitude scintillation seldom occurred in the high-latitude ionosphere [*Prikryl et al.*, 2010; *Moen et al.*, 2013; *Jin et al.*, 2014]. The details of the behavior of scintillations at the edges of different large-scale irregularities are not sufficiently explored. In this paper, we present a detailed comparison between the different irregularities and their associated scintillations and discuss the generated mechanisms by combining the observations of the global GPS TEC [*Coster et al.*, 2003], scintillations measured by Canadian High Arctic Ionospheric Network (CHAIN) [*Jayachandran et al.*, 2009], and the plasma flows observed by the SuperDARN radars [*Greenwald et al.*, 1995; *Chisham et al.*, 2007].

2. Data and Method

This study uses observations of the TEC from a dense array of ground-based GPS receivers, provided by the Madrigal database [*Coster et al.*, 2003]. A global TEC map is generated every 5 min, which can be used to continuously monitor the formation and evolution of the large-scale irregularities in the polar ionosphere [*Zhang et al.*, 2013a; *Thomas et al.*, 2013].

This study uses scintillation data observed by CHAIN, which is a network of 18 GPS ionospheric scintillation and TEC monitors (GISTM), model GSV4004B, in the northern part of Canada [*Jayachandran et al.*, 2009]. This provides a large coverage of scintillation measurements in this region. GISTM records the phase and amplitude of L1 band signals at 50 Hz and calculates amplitude and phase scintillations indices. The definition of amplitude scintillation index (S_4) is the standard deviation of the received signal power, normalized by the mean signal power over 60 s intervals. The phase scintillation index (σ_φ) is defined as the standard deviation of the carrier phase which has been detrended by a high-pass sixth-order Butterworth filter with a cutoff frequency of 0.1 Hz. σ_φ is calculated at time resolution of 1, 3, 10, 30, and 60 s. In this paper, the scintillation index with a time resolution of 60 s is used. The scintillation was classified into three grades: weak scintillation for S_4 (σ_φ) <0.3; moderate scintillation for $0.3 < S_4$ (σ_φ) <0.6; and strong scintillation for S_4 (σ_φ) >0.6. In order to avoid multipath effect, we have used data with elevation angle greater than 20° and signal locked time more than 240 s.

In order to make the comparison in large-scale areas, we have developed a tool to project both the GPS TEC and scintillations data at the Ionospheric Pierce Point (IPP) altitude of 350 km on a map of geomagnetic latitude (MLAT)/magnetic local time (MLT) grid in the northern polar ionosphere and generated a movie of the maps with 5 min resolution (e.g., Movies S1 and S2 in the supporting information). Thus, this time series of maps or movie will offer us a very good opportunity to pursue the detail comparison between the large-scale irregularities and the scintillations in the polar ionosphere.

The solar wind and interplanetary magnetic field (IMF) data are downloaded from the OMNI-2 website (mainly produced from the measurements of the Wind and ACE satellites in this study) [*King and Papitashvili*, 2005]. The solar wind data are time shifted to account for the distance from the satellites to the nose of bow shock.
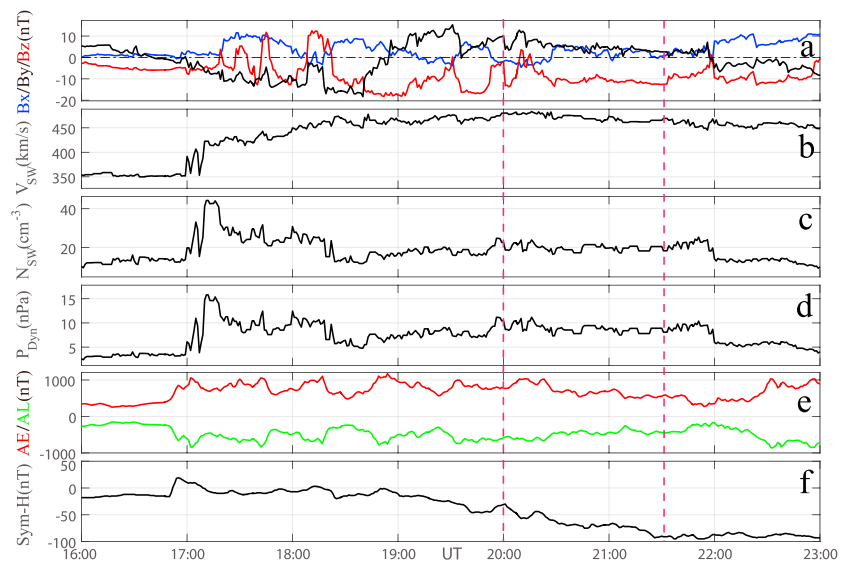
Figure 1. An overview of the solar wind and IMF conditions as well as the geomagnetic indices during the period 16:00–23:00 UT on 27 February 2014. Parameters are (a) the GSM IMF components, (b) the solar wind velocity, (c) the solar wind number density, (d) the solar wind dynamic pressure, P_{Dyn}, (e) the auroral electrojet (*AE/AL*) indices, and (f) the *SYM-H* (*Dst*) index. The IMF and solar wind data have been lagged by 7 min to allow for the propagation delay from the nose of bow shock to the polar ionosphere.

3. Observations and Results

3.1. Solar Wind and IMF Conditions and Geomagnetic Indices

On 27 February 2014, a coronal mass ejection (CME) reached the Earth magnetopause at about 17:00 UT with a shock in solar wind dynamic pressure, P_{Dyn}, resulting in a moderate geomagnetic storm. Figure 1 presents the solar wind and IMF conditions as well as the geomagnetic indices during 16:00–23:00 UT. Parameters are (a) the Geocentric Solar Magnetic (GSM) interplanetary magnetic field (IMF) components, (b) the solar wind velocity, (c) the solar wind number density, (d) the solar wind dynamic pressure, P_{Dyn}, (e) the auroral electrojet (*AE/AL*) indices, and (f) the *SYM-H* (*Dst*) index. The IMF and solar wind data have been lagged by 7 min to allow the data to propagate from the nose of the bow shock to the polar ionosphere. Before the CME impact (~17:00 UT), the IMF and solar wind conditions were weak and stable (Figures 1a–1d), resulting in quiet geomagnetic conditions (Figures 1e and 1f). After about 17:00 UT, however, the IMF and solar wind had strong variations (Figures 1a–1d), resulting in a series of substorms (Figure 1e) and a moderate geomagnetic storm (Figure 1f). The two vertical dashed lines highlight the interval of interest in this study. During this interval, the IMF B_z component was mainly negative around −10 nT with two positive excursions at about 20:10 UT and 20:15 UT, the B_y component was all positive and B_x varied around zero (see Figure 1a), while the solar wind was stable but kept high speed (~500 km/s) and number density (~20 cm^{-3}), giving a stable and high dynamic pressure (~10 nPa). These IMF conditions are favorable for reconnection at the dayside magnetopause. This interval was the period of the expansion phase to main phase of the storm with substorms at the beginning (Figures 1e and 1f).

3.2. Irregularities and Scintillations

Figure 2 shows selected examples from the movies of 2-D maps of ionospheric scintillations and TEC on a MLAT/MLT grid, where Figures 2a–2d are the maps of TEC and amplitude scintillations, and Figures 2e–2h are the maps of TEC and phase scintillations. The noon is on the top and the dusk is on left. The two black curves in each panel show the boundary with the sharpest flux gradient in the integral flux and the open/close boundary (OCB), respectively, which are predicted by the auroral Oval Variation Assessment Tracking Intensity and Online Nowcasting (OVATION) (shown in Figure 3a). The region highlighted by these two black curves represents the region with high integral flux for the precipitating electrons (shown in Figure 3a), generated by the Boundary-Oriented Precipitation Model [*Sotirelis and Newell*, 2000] and
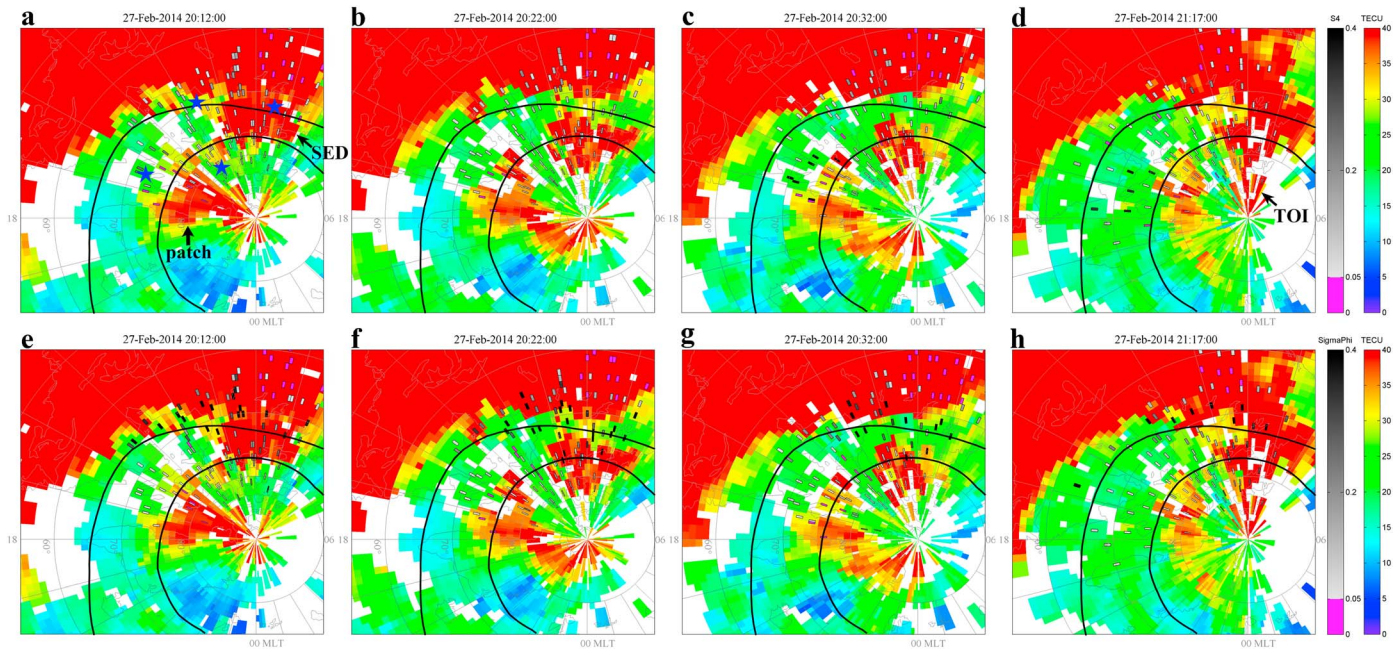
Figure 2. Selected examples from a full series of 2-D maps of median-filtered TEC and ionospheric scintillations on a MLAT/ MLT grid with noon at the top. (a–d) The maps of TEC and amplitude scintillations and (e–f) the maps of TEC and phase scintillations. The two black curves in each panel present the model predicted auroral oval determined by the intensity of the integral number flux of precipitating electrons (see detail in Figure 3a). There are two color bars for presenting the scintillation and TEC data, respectively.
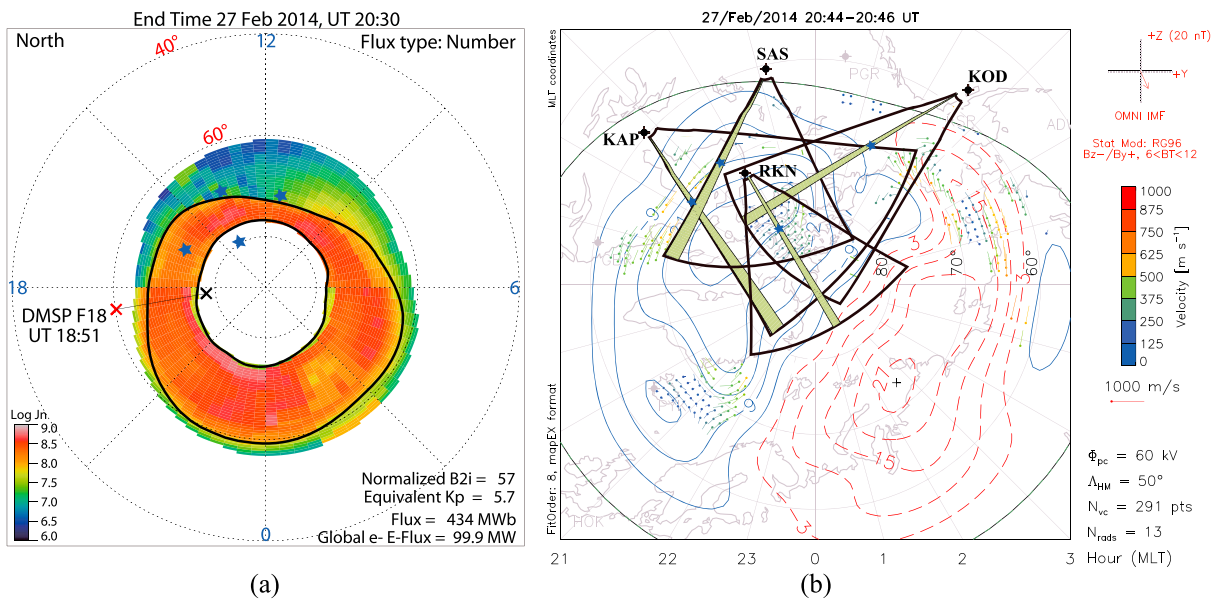

Figure 3. The 2-D maps of integral flux of precipitating electrons and of ionospheric convection pattern both on MLAT/MLT grid with noon at the top. The four blue stars show the selected points same as that in Figure 2a. (a) The modeled map of integral number flux in units of log10/(cm^2 sr s) from OVATION, which is predicted by the Boundary-Oriented Precipitation Model [*Sotirelis and Newell*, 2000] and calibrated in intensity by the DMSP magnetotail stretching index. The two black curves mark roughly the auroral oval boundaries, where the equatorward curve represents the boundary with the sharpest flux gradient and the poleward one shows the OCB. The thin black line with two "crosses" represents the projected orbit of DMSP F18, where the observations between the two crosses have been involved into the OVATION calibrations. The input and output parameters of the model inside OVATION are presented at the right-hand bottom corner of the map. (b) The field of view of the employed SuperDARN radars is projected in the map, which are presented as fans with the employed beam highlighted as the green area. The direction and magnitude of the lagged IMF are indicated at the right-hand upper corner of map.

calibrated in intensity by the DMSP magnetotail stretching index in OVATION. This region is roughly referred as the location of the auroral oval in this study. There are two color bars for each panel: the left one (grey) represents scintillation values from 0 to 0.4 (where values from 0 to 0.05 are considered as measurement/system noise and shown as magenta, and values above 0.4 were set as 0.4 for better comparison); the right one (color) represents TEC values between 0 and 40 TECU (1 TECU = 10^{16} el/m^2). Scintillation indices were represented by grey squares (and magenta squares indicating measurements at the noise level) with black frames in a size of 1° × 1° in MLAT and magnetic longitude (transferred to MLT in the map). The location of these squares represents the scintillations mapped to the Ionospheric Pierce Point (IPP) altitude of 350 km, where the scintillation values are averaged when they are filled in a same square. The TEC data downloaded from madrigal database have a spatial resolution of 1° × 1° in geographic latitude and geographic longitude. We transferred the TEC data into the altitude-adjusted corrected geomagnetic coordinates and performed the median-filtered average for smoothening them. The white area represents the TEC data gap. For better comparison with the 5 min averaged TEC data, we only selected the scintillation data at the middle of every 5 min, for example, selected the scintillation data at 20:22 UT for comparing the TEC data between 20:20–20:25 UT and 20:27 UT for that between 20:25 and 20:30 UT. At this end, we used this middle time as data time both for the TEC and scintillation data and presented it at the top of each panel.

From Figure 2, we identified three types of large-scale irregularities or regions from the TEC maps according to the TEC value and density gradient: SED, middle-latitude trough, and polar cap patches/TOI. A SED, as a plume of enhanced TEC, elongated from low-latitude afternoon sector toward high-latitude noon sector, entering the polar cap and forming a TOI (Figures 2a and 2e). And a clear middle-latitude trough, as the region of low TEC around 63–67° in the postnoon and premidnight sectors, convected toward the noon sector and encountered the SED plume at subauroral latitudes (Figures 2a and 2e). At about 20:22 UT (Figures 2b and 2f), a high-density plasma patch was completely formed pinching off from the SED plume/TOI at subauroral latitude (equatorward of the auroral oval) in the noon sector and the low-density plasma in the middle-latitude trough were transported to fill the gap between the patch and the left part of SED plume, while a previously formed patch was located deeper in the polar cap. After the formation, the polar cap patches moved poleward and duskward across the pole from dayside to nightside; however, the patches exited the polar cap and entered the auroral oval from very wide sectors ranging of about 15–23 MLT (see Figure 2 and Movies S1 and S2).

From Figure 2, we also find that clear amplitude and phase scintillations, shown by S_4 and σ_φ indices, appeared at the edges of these large-scale irregularities identified above. However, the behaviors of S_4 and σ_φ were different. σ_φ were much larger (blacker) than S_4 both in the segmenting area of the SED and at the equatorward edge of the middle-latitude trough in postnoon sector. S_4 and σ_φ were very small in the polar cap with similar magnitudes at the edges of polar cap patches, while S_4 were much larger than σ_φ in the auroral oval region around the exiting patches. These suggest that the generating mechanisms of the associated scintillations were different for different irregularities, which will be discussed in some detail in section 4.

4. Discussion

Based on the behaviors of the large-scale irregularities and the scintillations, we can divide the scintillation areas in the polar ionosphere into four typical regions: (1) the SED segmented area, (2) the middle-latitude trough, (3) the polar cap, and (4) the auroral oval. The auroral oval highlighted by the two black curves in Figure 2 comes from the modeled map of integral number flux and is characterized by high flux of precipitating electrons as shown in Figure 3a, where the equatorward curve represents the boundary with the sharpest flux gradient and the poleward one shows the OCB. Figure 3a is downloaded from OVATION, in which the distribution of the integral flux was generated by the Boundary-Oriented Precipitation Model [*Sotirelis and Newell*, 2000] and calibrated in intensity by the DMSP magnetotail stretching index. Figure 3a confirms that strong particle precipitations happened inside the auroral oval during the interval of interest.

In order to discuss the generating mechanisms of the associated scintillations in these four regions in detail, we selected four points from these regions around the edges of the large-scale irregularities or regions identified in section 3, shown as the blue stars in Figures 2a and 3, respectively. Around these selected points, the ionospheric flows can be monitored by the SuperDARN radars (Figure 3b). The SuperDARN radars can provide
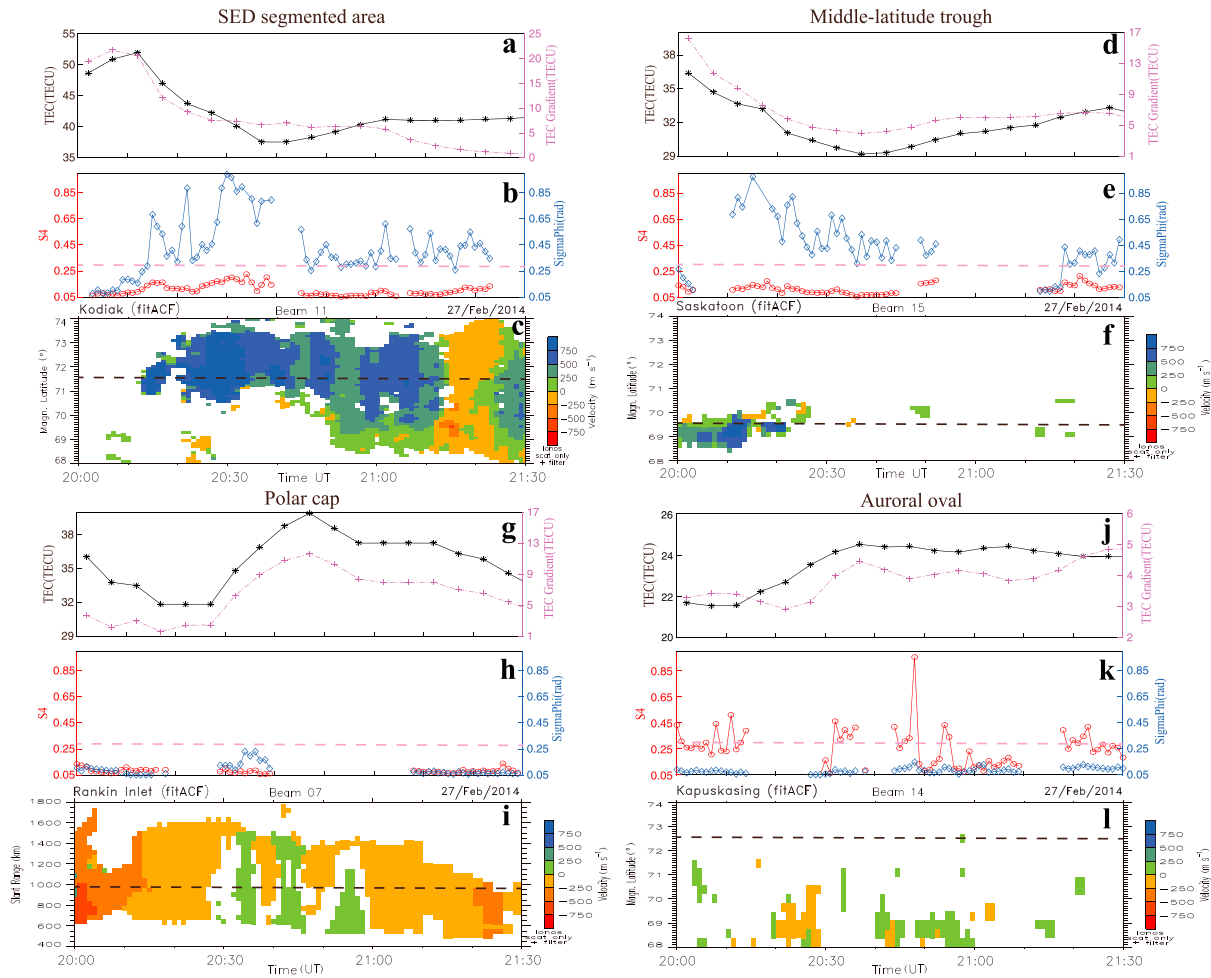
Figure 4. The time series of the TEC, TEC gradient, and scintillation data at the selected points for the four typical areas, together the line-of-sight velocity measured along the beams of SuperDARN radars which covered the selected points. The horizontal dashed lines represent the value of 0.3 in the scintillation indices panels and represent the corresponding positions of the selected points in the beams of the SuperDARN radars in the line-of-sight velocity panels.

convection patterns in the whole polar ionosphere by using the "Map Potential" technique [*Ruohoniemi and Baker*, 1998; *Chisham et al.*, 2007], while the individual radars can offer us the line-of-sight velocity around the regions of interest. These will offer us the opportunity to check the flow variations around the selected points. Figure 3b shows the SuperDARN convection map and the field of view of the SuperDARN Kodiak (KOD), Saskatoon (SAS), Rankin Inlet (RKN), and Kapuskasing (KAP) radars with the beams covering the four selected points (blue stars). A typical two-cell convection pattern was shown with the observed drift vectors in Figure 3b for southward IMF condition, which was varying with the inputting IMF conditions. The line-of-sight velocities are shown in Figure 4 along the highlighted beams covering the selected points, where the missing data are meaning no target presenting from which the radar could scatter, due to HF absorption and/or lack of irregularities [*Moen et al.*, 2001].

We extracted a time series of the TEC and scintillation data around the selected points from the maps in Figure 2 and Movies S1 and S2 and also presented them in Figure 4. In order to obtain the time series of the spatial density gradient at each selected point, we chose another point as a reference to calculate the TEC difference between it and the selected point. The reference points are 2° higher in MLAT than the selected points along the same MLT as these selected points, except for the one in the polar cap, which is 0.4 h higher in MLT than the selected point along the same MLAT with this selected point. Because the scintillation data have very poor spatial coverage (seen in Figure 2), the time series of scintillation data has been searched and averaged from a 3×3 points data matrix which represents a $3° \times 0.4$ MLAT/MLT grid centered by the selected point in the map.

Below, we discuss the generating mechanisms of the scintillation in these four typical regions mentioned above, respectively, but discuss the regions 1 and 2 together because the SED segmented area and the middle-latitude trough link together and have similar scintillation behaviors.

4.1. SED Segmented Area and the Middle-Latitude Trough

The SED plume was drifted from low-latitude afternoon sector toward high-latitude noon sector by the poleward directed SAPS electric fields, entering the polar cap and forming a TOI [*Foster*, 2008]. *Zhang et al.* [2013a, 2015] found that these bursty sunward return flows or SAPS could carry low-density plasma (trough) toward the cusp region along the dawnside and/or duskside return convection cell, thereby injecting low-density plasma into the convection throat and cutting the SED plume into polar cap patches [*Moen et al.*, 2006; *Goodwin et al.*, 2015]. In Figure 2, the low-density plasma in the middle-latitude trough was indeed transported to fill the gap between the patch and the left part of SED plume. This is more visible in Figure 4a, where the TEC value increased to 52 TECU when the SED plume generally reached the selected point from lower latitudes and then decreased to 37 TECU when the lower density plasma from the trough filled the gap of the SED segmented area, resulting very strong density gradients (more than 10 TECU) at the poleward edge of the SED plume. The scintillation data at the selected point show that the phase scintillations were always stronger than the amplitude scintillations (S_4 is very small, $<\sim 0.2$) (Figure 4b). The scintillations were small with similar magnitude of S_4 and σ_φ during SED plume approaching the selected point (before the TEC reaching the maximum in Figure 4a), while the phase scintillations were strongly enhanced when the low-density plasma in middle-latitude trough pinched off the leading part of the SED between 20:12 and 20:52 UT: σ_φ were all above 0.3 with several times above 0.6 and reaching their maximum of 0.9; and σ_φ were decreased to about 0.3 with some small enhancements during the periods of 20:59–21:23 UT, when the left part of the SED plume propagating toward the selected point (Figure 4b). The line-of-sight flows show that there were bursty flows or SAPS (~1000 m/s) toward (sunward) the SuperDARN Kodiak radar during the periods of 20:12–20:42 UT, 20:48–20:52 UT, and 20:58–21:12 UT, with a short time flow reversal (away from the radar) during 21:16–21:24 UT (Figure 4c). From Figures 4a–4c, we can find that the scintillation enhanced was associated with the bursty flows and the flow reversal. Note that during the period of 20:51–20:58 UT, the flows were not strong (~500 m/s), the phase scintillation well less pronounced (σ_φ varied around 0.3) compared to the previous periods, which may be because low flow speed and the low-density plasma fully filled the segmented area with very small density gradient. These observations suggest that these strong phase scintillations, which were thought to be generated by the small-scale irregularities with sizes of hundreds of meters to some kilometers pinching off from the SED plume [e.g., *Kintner et al.*, 2007; *van der Meeren et al.*, 2014], were mainly associated with the bursty flows or flow reversal, although there are also strong density gradients at the edges of the segmenting area between the SED and the newly created patch (mainly at the leading edge of the left part of the SED and the equatorward edge of the newly created patch).

In the postnoon middle-latitude trough, the TEC and their gradient showed that the trough was extension equatorward with strong density gradient (Figure 4d), and the phase scintillations were almost always much stronger than the amplitude scintillations (Figure 4e). During the equatorward extending, the bursty flows or SAPS were also measured in the trough by the SuperDARN Saskatoon radar, although the radar backscatter echo was rare after about 20:28 UT which may be due to the radar signal be absorbed and/or lack of irregularities in the trough region (Figure 4f) [*Moen et al.*, 2001]. Similar to that within the SED segmented area, these observations also suggest that the strong phase scintillation was mainly generated by the small-scale irregularities associated with the bursty flows at the equatorward edge of the middle-latitude trough.

4.2. Polar Cap

After segmented from the SED plume, the patches moved by following the flow streamlines and entered the polar cap region. This type of segmented process was pulsed due to injection of the bursty sunward return flows or SAPS associated with pulsed nightside reconnections; thus, the patch appeared one following another and may be further structured by the GDI during their evolution in the polar cap [*Carlson et al.*, 2007; *Spicher et al.*, 2015]. In Figures 4g–4i, a polar cap patch appeared across the selected point with strong density gradient, while during the whole interval, both the amplitude and phase scintillations were very weak (both S_4 and σ_φ were below ~0.3) with some small enhancements between 20:32 and 20:39 UT in phase

scintillations, when the line-of-sight flows was reversed within the background of weak flows (~ −200 m/s). These observations suggest that the scintillations were very weak in the polar cap but would be enhanced by the varied flows with the density gradient at the edges of the polar cap patches.

4.3. Auroral Oval

After transpolar evolution across the pole from dayside to nightside, the patches exited the polar cap and entered the auroral oval in very wide sectors ranging of about 15–23 MLT (see Figure 2 and Movies S1 and S2). This may be due to the nightside reconnection occurred at very wide regions from the dusk flank to the premidnight sectors of the magnetotail, which modulated the patches exiting the polar cap region [*Zhang et al.*, 2013a, 2015; *Moen et al.*, 2007, 2015]. These nightside reconnections reclosed the open field lines in the lobe region and generated particle precipitations into the polar ionosphere along the newly closed field lines during their sunward moving from dawn/dusk flank driven by the convection electric field, forming the auroral oval. Thus, the patches will be affected by the particle precipitations when they exit the polar cap region and enter the nightside auroral oval. In Figures 4j–4l, the TEC and their gradient show that there were several small gradient enhancements (only about 3–4 TECU) during the periods of about 20:00–20:15, 20:27–20:42, 20:50–21:02, and 21:12–21:30 UT, when the patch crossed the selected point in the auroral oval, which may be due to the particle precipitations. On the other hand, Figure 3a shows that there are strong particle precipitations around the selected point suggested by the modeled integral flux from OVATION and plasma observations from DMSP. During this interval, the scintillation data show an unexpected feature that the amplitude scintillations became dominant and increased above 0.3 when the density gradient showed enhancement, while the phase scintillations were very weak during the whole interval. These observations and modeled results suggested that the particle precipitations might play the main role to generate a series of small-scale irregularities in the sizes from tens of meters to hundreds of meters around the patch, which therefore produced clear amplitude scintillations in the auroral oval.

5. Conclusions

We developed a tool to project the global GPS TEC and large coverage of ionospheric scintillations together on the map of MLAT/MLT grid. Using this tool, we have made a detailed comparison between large-scale irregularities and scintillations in the polar ionosphere during a geomagnetic storm and identify clear irregularities from the global GPS TEC: the SED plume, the middle-latitude trough, and polar cap patches. At the edges of these irregularities, scintillations were apparently recorded but their behaviors were different. Based on the behaviors of the scintillations, we divided the scintillation areas in four typical regions: (1) the SED segmented area, (2) the middle-latitude trough, (3) the polar cap, and (4) the auroral oval. Both in the SED segmented area and at the equatorward edge of the middle-latitude trough in postnoon sector, the phase scintillations were much larger than amplitude scintillations associated with the bursty flows or flow reversals. In the polar cap, both the amplitude and phase scintillations were very weak with small enhancements due to the varied flows with the density gradient at the edges of polar cap patches. An unexpected scintillation feature appeared inside the auroral oval, where amplitude scintillations were much larger than phase scintillations, most likely caused by particle precipitations around the exiting patches. The results offer a key opportunity for improving polar ionospheric modeling and Global Navigation Satellite System (GNSS) scintillation forecasts.

References

Alfonsi, L., L. Spogli, G. De Franceschi, V. Romano, M. Aquino, A. Dodson, and C. N. Mitchell (2011), Bipolar climatology of GPS ionospheric scintillation at solar minimum, *Radio Sci.*, 46, RS0D05, doi:10.1029/2010RS004571.

Basu, S., S. Basu, E. MacKenzie, W. R. Coley, J. R. Sharber, and W. R. Hoegy (1990), Plasma structuring by the gradient drift instability at high latitudes and comparison with velocity shear driven processes, *J. Geophys. Res.*, 95, 7799–7818, doi:10.1029/JA095iA06p07799.

Basu, S., S. Basu, P. K. Chaturvedi, and C. M. Bryant (1994), Irregularity structures in the cusp/cleft and polar cap regions, *Radio Sci.*, 29, 195–207, doi:10.1029/93RS01515.

Basu, S., E. J. Weber, T. W. Bullett, M. J. Keskinen, E. MacKenzie, P. Doherty, R. Sheehan, H. Kuenzler, P. Ning, and J. Bongiolatti (1998), Characteristics of plasma structuring in the cusp/cleft region at Svalbard, *Radio Sci.*, 33, 1885–1899, doi:10.1029/98RS01597.

Carlson, H. C. (2012), Sharpening our thinking about polar cap ionospheric patch morphology, research, and mitigation techniques, *Radio Sci.*, 47, RS0L21, doi:10.1029/2011RS004946.

Carlson, H. C., T. Pedersen, S. Basu, M. Keskinen, and J. Moen (2007), Case for a new process, not mechanism, for cusp irregularity production, *J. Geophys. Res.*, 112, A11304, doi:10.1029/2007JA012384.

Chisham, G., et al. (2007), A decade of the Super Dual Auroral Radar Network (SuperDARN): Scientific achievements, new techniques and future directions, *Surv. Geophys.*, 28, 33–109, doi:10.1007/s10712-007-9017-8.

Coster, A., J. Foster, and P. Erickson (2003), Monitoring the Ionosphere with GPS space weather, *GPS World*, 14(5), 42.

Crowley, G. (1996), Critical review of ionospheric patches and blobs, in *Review of Radio Science 1992-1996*, edited by W. R. Stone, pp. 619–648, Oxford Univ. Press, Oxford, U. K.

De Franceschi, G., L. Alfonsi, V. Romano, M. Aquino, A. Dodson, C. N. Mitchell, P. Spencer, and A. W. Wernik (2008), Dynamics of high-latitude patches and associated small-scale irregularities during the October and November 2003 storms, *J. Atmos. Sol. Terr. Phys.*, 70, 879–888, doi:10.1016/j.jastp.2007.05.018.

Dungey, W. J. (1961), The steady state of the Chapman-Ferraro problem in two dimensions, *J. Geophys. Res.*, 66, 1043–1047, doi:10.1029/JZ066i004p01043.

Foster, J. C. (2008), Ionospheric-magnetospheric-heliospheric coupling: Storm-time thermal plasma redistribution, in *Midlatitude Ionospheric Dynamics and Disturbances*, vol. 181, edited by P. M. Kintner Jr. et al., pp. 121–134, AGU, Washington, D. C., doi:10.1029/181GM12.

Foster, J. C., and W. J. Burke (2002), SAPS: A new characterization for sub-auroral electric fields, *Eos Trans. AGU*, 83(36), 393–394, doi:10.1029/2002EO000289.

Foster, J. C., et al. (2005), Multiradar observations of the polar tongue of ionization, *J. Geophys. Res.*, 110, A09S31, doi:10.1029/2004JA010928.

Foster, J. C., W. Rideout, B. Sandel, W. T. Forrester, and F. J. Rich (2007), On the relationship of SAPS to storm-enhanced density, *J. Atmos. Sol. Terr. Phys.*, 69, 303–313, doi:10.1016/j.jastp.2006.07.021.

Goodwin, L. V., et al. (2015), Swarm in situ observations of F region polar cap patches created by cusp precipitation, *Geophys. Res. Lett.*, 42, 996–1003, doi:10.1002/2014GL062610.

Greenwald, R. A., W. A. Bristow, G. J. Sofko, C. Senior, J.-C. Cerisier, and A. Szabo (1995), Super dual auroral radar network radar imaging of dayside high-latitude convection under northward interplanetary magnetic field: Toward resolving the distorted two-cell versus multicell controversy, *J. Geophys. Res.*, 100, 19,661–19,674, doi:10.1029/95JA01215.

Hey, J. S., S. J. Parsons, and J. W. Phillips (1946), Fluctuations in cosmic radiation at radio-frequencies, *Nature*, 158, 234.

Hosokawa, K., K. Shiokawa, Y. Otsuka, T. Ogawa, J.-P. St-Maurice, G. J. Sofko, and D. A. Andre (2009), Relationship between polar cap patches and field-aligned irregularities as observed with an all-sky airglow imager at Resolute Bay and the PolarDARN radar at Rankin Inlet, *J. Geophys. Res.*, 114, A03306, doi:10.1029/2008JA013707.

Jayachandran, P. T., et al. (2009), Canadian High Arctic Ionospheric Network (CHAIN), *Radio Sci.*, 44, RS0A03, doi:10.1029/2008RS004046.

Jin, Y., J. Moen, and W. J. Miloch (2014), GPS scintillation effects associated with polar cap patches and substorm auroral activity: Direct comparison, *J. Space Weather Space Clim.*, 4, A23, doi:10.1051/SWSC/2014019.

Jin, Y., J. Moen, and W. J. Miloch (2015), On the colocation of the cusp aurora and the GPS phase scintillation: A statistical study, *J. Geophys. Res. Space Physics*, 120, 9176–9191, doi:10.1002/2015JA021449.

King, J. H., and N. E. Papitashvili (2005), Solar wind spatial scales in and comparisons of hourly Wind and ACE plasma and magnetic field data, *J. Geophys. Res.*, 110, A02104, doi:10.1029/2004JA010649.

Kintner, P. M., B. M. Ledvina, and E. R. de Paula (2007), GPS and ionospheric scintillations, *Space Weather*, 5, S09003, doi:10.1029/2006SW000260.

Mitchell, C. N., L. Alfonsi, G. De Franceschi, M. Lester, V. Romano, and A. W. Wernik (2005), GPS TEC and scintillation measurements from the polar ionosphere during the October 2003 storm, *Geophys. Res. Lett.*, 32, L12S03, doi:10.1029/2004GL021644.

Moen, J., H. C. Carlson, S. E. Milan, N. Shumilov, B. Lybekk, P. E. Sandholt, and M. Lester (2001), On the collocation between dayside auroral activity and coherent HF radar backscatter, *Ann. Geophys.*, 18, 1531–1549.

Moen, J., H. C. Carlson, K. Oksavik, C. P. Nielsen, S. E. Pryse, H. R. Middleton, I. W. McCrea, and P. Gallop (2006), EISCAT observations of plasma patches at sub-auroral cusp latitudes, *Ann. Geophys.*, 24, 2363–2374.

Moen, J., N. Gulbrandsen, D. A. Lorentzen, and H. C. Carlson (2007), On the MLT distribution of F-region polar cap patches at night, *Geophys. Res. Lett.*, 34, L14113, doi:10.1029/2007GL029632.

Moen, J., K. Oksavik, L. Alfonsi, Y. Daabakk, V. Romano, and L. Spogli (2013), Space weather challenges of the polar cap ionosphere, *J. Space Weather Space Clim.*, 3, A02, doi:10.1051/SWSC/2013025.

Moen, J., K. Hosokawa, N. Gulbrandsen, and L. B. N. Clausen (2015), On the symmetry of ionospheric polar cap patch exits around magnetic midnight, *J. Geophys. Res. Space Physics*, 120, 7785–7797, doi:10.1002/2014JA020914.

Oksavik, K., V. L. Barth, J. Moen, and M. Lester (2010), On the entry and transit of high-density plasma across the polar cap, *J. Geophys. Res.*, 115, A12308, doi:10.1029/2010JA015817.

Oksavik, K., C. van der Meeren, D. A. Lorentzen, L. J. Baddeley, and J. Moen (2015), Scintillation and loss of signal lock from poleward moving auroral forms in the cusp ionosphere, *J. Geophys. Res. Space Physics*, 120, 9161–9175, doi:10.1002/2015JA021528.

Prikryl, P., P. T. Jayachandran, S. C. Mushini, D. Pokhotelov, J. W. MacDougall, E. Donovan, E. Spanswick, and J.-P. St.-Maurice (2010), GPS TEC, scintillation and cycle slips observed at high latitudes during solar minimum, *Ann. Geophys.*, 28(6), 1307–1316, doi:10.5194/angeo-28-1307-2010.

Ruohoniemi, J. M., and K. B. Baker (1998), Large-scale imaging of high-latitude convection with SuperDARN HF radar observations, *J. Geophys. Res.*, 103, 20,797–20,811, doi:10.1029/98JA01288.

Sotirelis, T., and P. T. Newell (2000), Boundary-oriented electron precipitation model, *J. Geophys. Res.*, 105, 18,655–18,673, doi:10.1029/1999JA000269.

Spicher, A., T. Cameron, E. M. Grono, K. N. Yakymenko, S. C. Buchert, L. B. N. Clausen, D. J. Knudsen, K. A. McWilliams, and J. I. Moen (2015), Observation of polar cap patches and calculation of gradient drift instability growth times: A Swarm case study, *Geophys. Res. Lett.*, 42, 201–206, doi:10.1002/2014GL062590.

Thomas, E. G., J. B. H. Baker, J. M. Ruohoniemi, L. B. N. Clausen, A. J. Coster, J. C. Foster, and P. J. Erickson (2013), Direct observations of the role of convection electric field in the formation of a polar tongue of ionization from storm enhanced density, *J. Geophys. Res. Space Physics*, 118, 1180–1189, doi:10.1002/jgra.50116.

van der Meeren, C., K. Oksavik, D. Lorentzen, J. I. Moen, and V. Romano (2014), GPS scintillation and irregularities at the front of an ionization tongue in the nightside polar ionosphere, *J. Geophys. Res. Space Physics*, 119, 8624–8636, doi:10.1002/2014JA020114.

Weber, E. J., J. A. Klobuchar, J. Buchau, H. C. Carlson Jr., R. C. Livingston, O. de la Beaujardiere, M. McCready, J. G. Moore, and G. J. Bishop (1986), Polar cap F layer patches: Structure and dynamics, *J. Geophys. Res.*, 91, 12,121–12,129, doi:10.1029/JA091iA11p12121.

Zhang, Q.-H., et al. (2011), On the importance of interplanetary magnetic field |By| on polar cap patch formation, *J. Geophys. Res.*, 116, A05308, doi:10.1029/2010JA016287.

Zhang, Q.-H., et al. (2013a), Direct observations of the evolution of polar cap ionization patches, *Science*, 339, 1597–1600, doi:10.1126/science.1231487.

Zhang, Q.-H., B.-C. Zhang, J. Moen, M. Lockwood, I. W. McCrea, H.-G. Yang, H.-Q. Hu, R.-Y. Liu, S-R. Zhang, and M. Lester (2013b), Polar cap patch segmentation of the tongue of ionization in the morning convection cell, *Geophys. Res. Lett.*, 40, 2918–2922, doi:10.1002/grl.50616.

Zhang, Q.-H., M. Lockwood, J. C. Foster, S-R. Zhang, B.-C. Zhang, I. W. McCrea, J. Moen, M. Lester, and J. M. Ruohoniemi (2015), Direct observations of the full Dungey convection cycle in the polar ionosphere for southward interplanetary magnetic field conditions, *J. Geophys. Res. Space Physics*, 120, 4519–4530, doi:10.1002/2015JA021172.